






Tailoring the aluminum nanocrystal surface oxide for all-aluminum-based antenna-reactor plasmonic photocatalysts

Aaron Bayles^{a,b}, Catherine J. Fabiano^c, Chuqiao Shi^d, Lin Yuan^{a,b}, Yigao Yuan^{a,b}, Nolan Craft^e, Christian R. Jacobson^{a,b}, Parmeet Dhindsa^{a,b}, Adebola Ogundare^{a,b}, Yelsin Mendez Camacho^d, Banghao Chen^c, Hossein Robatjazi^a, Yimo Han^d, Geoffrey F. Strouse^c, Peter Nordlander^{b,e} , Henry O. Everitt^{a,b,e,f,g} , and Naomi J. Halas^{a,b,e,f,1} 

Contributed by Naomi J. Halas; received December 15, 2023; accepted January 24, 2024; reviewed by Alexandra Boltasseva and Michelle Pantoya

Aluminum nanocrystals (AINCs) are of increasing interest as sustainable, earth-abundant nanoparticles for visible wavelength plasmonics and as versatile nanoantennas for energy-efficient plasmonic photocatalysis. Here, we show that annealing AINCs under various gases and thermal conditions induces substantial, systematic changes in their surface oxide, modifying crystalline phase, surface morphology, density, and defect type and concentration. Tailoring the surface oxide properties enables AINCs to function as all-aluminum-based antenna-reactor plasmonic photocatalysts, with the modified surface oxides providing varying reactivities and selectivities for several chemical reactions.

aluminum | alumina | surface oxide

Alumina is a highly versatile material, with applications as diverse as catalyst supports, cutting tools, and surgical implants (1–5). In addition to its stable α - Al_2O_3 phase, alumina can exist in a range of metastable “transition alumina” phases, each with unique properties, allowing specific alumina phases to be selected for a given application (6, 7). For example, η - and γ -aluminas are used as catalyst supports for alcohol dehydration and hydrogen sulfide decomposition (the Claus process) due to their hydrothermal stability, controllable surface area, rich defect chemistry, and the presence of both acidic and basic surface sites (8–10). However, the wide bandgap of the various alumina polymorphs, nominally 7 eV, has precluded their use in photocatalysis.

Leveraging the versatile surface chemistry of the aluminas for visible photocatalysis requires a new approach. One particularly attractive strategy would be to use an alumina polymorph with catalytically active surface sites as a reactor, in combination with the light-harvesting properties and nonequilibrium processes of a plasmonic antenna (11). Plasmonic antenna-reactor photocatalysis is of rapidly growing interest and importance because it can dramatically lower the effective activation energy of multiple chemical reactions, enabling highly endothermic reactions to proceed without an external heat source (12–14). Coinage metals such as Au, Ag, or Cu that sustain localized surface plasmons make outstanding optical antennas for photocatalysis. Aluminum, the most abundant metal in the Earth’s crust, supports a size- and morphology-tunable plasmon resonance, making it a promising and sustainable optical antenna material (15, 16). Aluminum nanocrystals (AINCs) have recently been demonstrated as plasmonic photocatalysts and as antennas in antenna-reactor photocatalytic complexes for reactions such as methanol decomposition and acetylene hydrogenation (17, 18). A thin (~4 nm), self-limiting native oxide grows on the AINC surface, protecting it from further uncontrolled oxidation and degradation under ambient conditions (19).

Here, we demonstrate all-aluminum-based plasmonic antenna-reactor photocatalysts, nanoparticle complexes composed of an Al core and different transition alumina polymorphs with their corresponding active sites. Thermal annealing of colloiddally synthesized AINCs under various conditions controllably modifies the surface alumina, transforming several properties of the native oxide. We examine how this approach modulates oxide porosity and coordination environment, altering surface chemistry, strain, and catalytic properties. By comparing plasmonic photocatalytic activity of AINCs under three different annealing conditions, we observe that photocatalytic activity is dependent upon defect density and type. The modified oxide can provide electron traps for reactions favoring basic surfaces or, by enhancing the crystallinity of the surface oxide, can reduce the density of chemically reactive trap states compared to trap-rich surface oxides. The ability to modify AINC surface oxide properties by such a straightforward annealing step enables a surprisingly wide range of chemistries that can be facilitated by this all-Al antenna-reactor plasmonic photocatalyst complex.

Significance

Aluminum is an earth-abundant metal used in a great many structural and technological applications. All aluminum is terminated with a surface oxide; it is the properties of this alumina layer that govern the interactions of aluminum with molecules and materials. Here, we show that the alumina layer surrounding aluminum nanocrystals can be altered in multiple ways by annealing the nanocrystals in various chemical ambients. The crystalline phase, type of defect, and defect density can all be modified by this straightforward approach. Changing the alumina layer in this manner affects its catalytic properties, particularly for light-driven chemical reactions where the aluminum nanocrystal core acts as an optical frequency antenna and the defects induced in the aluminum surface oxide play the role of reactive sites.

Author contributions: H.R., Y.H., P.N., H.O.E., and N.J.H. designed research; A.B., C.J.F., C.S., L.Y., Y.Y., N.C., C.R.J., P.D., A.O., Y.M.C., and B.C. performed research; A.B., C.J.F., H.R., Y.H., and H.O.E. analyzed data; and A.B., C.J.F., C.S., H.R., Y.H., G.F.S., P.N., H.O.E., and N.J.H. wrote the paper.

Reviewers: A.B., Purdue University West Lafayette; and M.P., Texas Tech University.

The authors declare no competing interest.

Copyright © 2024 the Author(s). Published by PNAS. This article is distributed under [Creative Commons Attribution-NonCommercial-NoDerivatives License 4.0 \(CC BY-NC-ND\)](https://creativecommons.org/licenses/by-nc-nd/4.0/).

¹To whom correspondence may be addressed. Email: halas@rice.edu.

This article contains supporting information online at <https://www.pnas.org/lookup/suppl/doi:10.1073/pnas.2321852121/-DCSupplemental>.

Published March 5, 2024.

Results

AINCs were synthesized in an Ar-filled glovebox following a previously described procedure (20), purified by centrifugation, and then dried in a vacuum desiccator. Upon exposure to ambient postsynthesis, the pristine AINCs react with ambient atmosphere to grow an ultrathin, self-limiting native oxide, which can be observed using energy-dispersive X-ray (EDX) imaging (Fig. 1*A*). The amorphous nature of the native oxide can be confirmed by an apparent lack of sharp oxide peaks in its X-ray diffraction spectrum (XRD, *SI Appendix*, Fig. S1). The AINCs were annealed at 500 °C for 60 min under three different ambient conditions: A) low vacuum ($\sim 10^{-2}$ torr), B) ultrahigh purity helium, or C) 10% oxygen in helium atmosphere. Following these annealing protocols, EDX measurements showed that all samples retained their essential morphology (Fig. 1*B–D*). The He-annealed AINCs retained a similar oxide percentage relative to the unannealed AINCs, the O₂-annealed AINCs exhibited a significantly higher percentage of oxide, strongest at the AINC edges, and the vacuum-annealed samples also appeared to have a greater oxygen content, indicating a thicker oxide shell. This was confirmed by EDX analysis which also showed an increased atomic fraction of oxygen for O₂- and vacuum-annealed AINCs (Fig. 1*E* and *SI Appendix*, Fig. S2).

Transmission Electron Microscopy Imaging. To examine the morphology of the various oxide layers with greater resolution, high-resolution transmission electron microscopy (HRTEM) imaging was performed. Several significant changes in oxide thickness and properties upon application of various annealing conditions were observed. He-annealed particles possess a characteristic ~ 4 -nm alumina shell, while O₂-annealed and vacuum-annealed AINCs possess oxide layers of 11 ± 2.2 nm and 7.6 ± 1.2 nm thickness, respectively (Fig. 1*F–I* and *SI Appendix*, Fig. S3). While the native oxide thickness was unchanged by He annealing relative to the unannealed case, the substantially increased thickness of the O₂-annealed AINCs is likely due to oxidation of the AINC core during the annealing process. The increased thickness of the vacuum-annealed AINCs likely originates from a weaker oxidation of the AINC core due to the lower oxygen content of its annealing ambient, followed by subsequent air-ambient exposure. For the

vacuum-annealed case, there is a distinct surface roughness observable at the oxide–air interface not present for AINCs that have undergone other annealing treatments (Fig. 1*I*).

All AINCs possess a crystalline metallic core with a 4.04 Å lattice spacing. The alumina layer of the O₂-annealed AINCs also exhibits a crystalline lattice, with a 3.90 Å lattice constant (*SI Appendix*, Fig. S4), while the other annealing conditions yielded amorphous oxide shells. This is confirmed by XRD measurements, where the well-defined Al oxide peaks at 46° and 67° are only observed for O₂-annealed AINCs (*SI Appendix*, Fig. S5) (21). By lengthening the O₂ annealing time, the intensity of the oxide XRD peaks increased at the expense of the metal peaks (Fig. 2*A*), confirming that the crystalline oxide shell grows and the oxide mass ratio (ratio of oxide to metal) increases as the Al core is oxidized (Fig. 2*A*, *Inset*). The metal peaks progressively shift to lower angles, indicating increasing Al core strain (Fig. 2*A*, *Inset*); HRTEM reveals Moiré fringe patterns radiating from the oxide–metal interface due to strain induced in the Al core by surface oxide crystallization and the resulting lattice mismatch (Fig. 2*B*).

The degree of crystallinity and intraparticle strain induced by O₂ annealing was investigated in further detail using 4D-Scanning TEM (4D-STEM) (22, 23). Al nanocubes were synthesized following a previously described procedure (24), annealed in O₂, and compared to O₂-annealed twinned particles. High-angle annular dark field (HAADF) STEM images revealed particles of both morphologies to have a thicker oxide shell while overall particle shape was conserved. (Fig. 2*C* and *D*). Fluctuation Electron Microscopy (FEM) allows for crystallinity information to be extracted from a 4D-STEM dataset, in which higher intensity correlates to higher crystallinity (25). Interestingly, while both twinned and nanocube particles demonstrate a highly crystalline core, the twinned particle surface oxide is primarily crystalline while the cube surface oxide appears substantially more amorphous (Fig. 2*E* and *F*). This is attributed to the possibility that the {100} facets of the cube may potentially frustrate oxide crystallization, an observation that merits further study. The nanocube core appears distorted after annealing when compared to an unannealed nanocube (*SI Appendix*, Fig. S6) due to preferential oxidation at its vertices. Strain mapping reveals the presence of strain variation across the oxide and core of the twinned particle, which arises from lattice distortion near the metal-oxide interface (Fig. 2*G*).

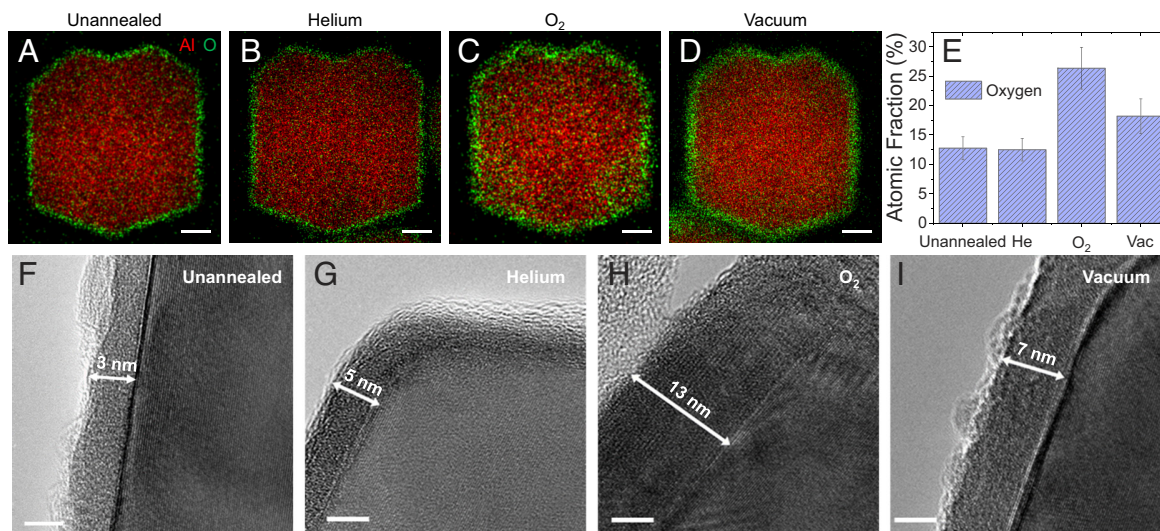


Fig. 1. Morphologies of AINC surface oxides that have undergone different annealing protocols. EDX elemental mapping of (A) unannealed, (B) He-annealed, (C) O₂-annealed, and (D) vacuum-annealed single AINCs. Al is red, O is green, and scale bars are 50 nm. (E) EDX atomic fraction of oxygen for each sample. (F–I) HRTEM of AINC oxide layers. The measured oxide thickness is marked. (Scale bars are 5 nm.)

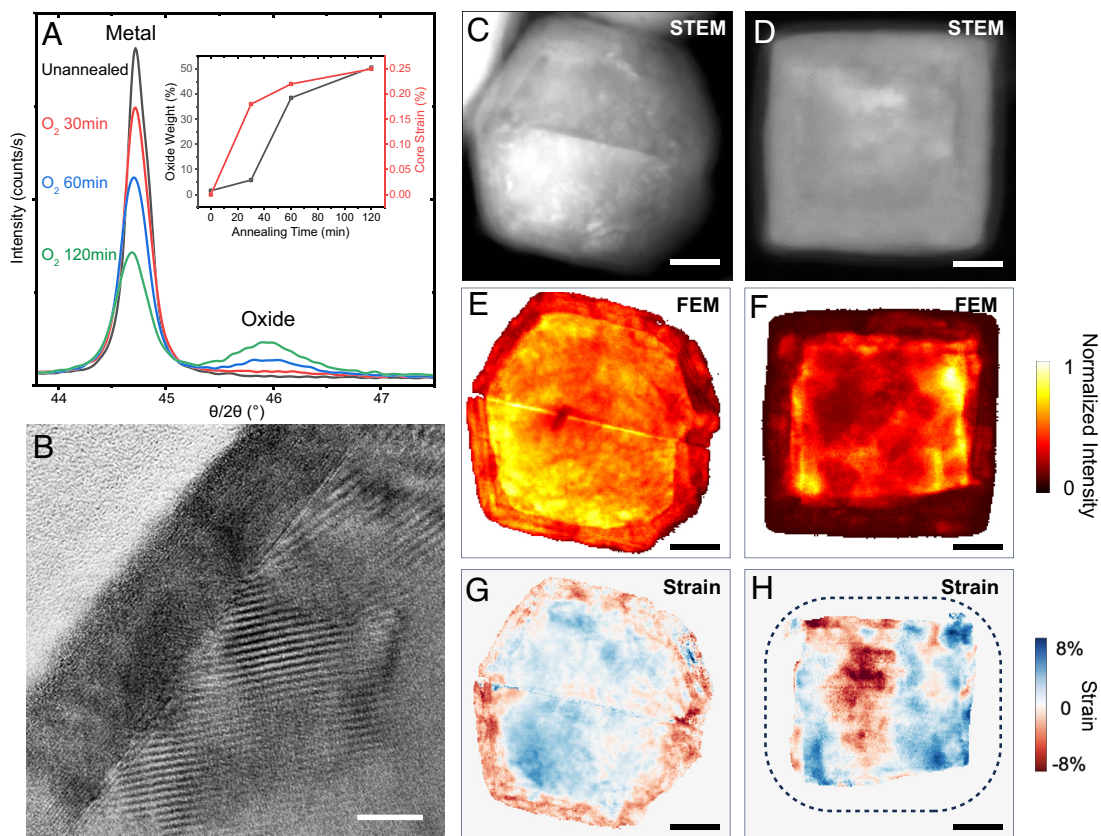


Fig. 2. Structural and strain mapping analysis of O_2 -annealed AlNCs. (A) XRD of AlNCs unannealed and annealed in O_2 for different times. (Inset) Oxide weight ratio and Al core strain calculated from the XRD peak analysis. (B) HRTEM of the edge of a cuboctahedron particle following O_2 annealing, demonstrating additional strain-induced fringe patterns radiating from metal-oxide interface. The scale bar is 10 nm. HAADF-STEM image of an O_2 -annealed (C) twinned AlNC and (D) Al nanocube. (E and F) Corresponding FEM maps for the twinned particle particles. (G and H) Corresponding strain maps for the twinned and cube particles. Dashed outline of cube represents the approximate location of the surface oxide-vacuum interface. (Scale bars are 20 nm.)

The Al nanocube images suggest that the core also undergoes residual strain, although the amorphous character of the oxide precludes the ability to extract strain information from that region (Fig. 2H). Images of the He-, and Vac-annealed AlNCs reveal low core strain (SI Appendix, Fig. S7).

Plasmonic Properties. Individual nanoparticle dark-field scattering spectra provide information regarding how annealing affects the plasmonic properties of the AlNCs (ensemble extinction spectra shown in SI Appendix, Fig. S8). The annealing process induces two primary trends that can modify the plasmon resonance frequency in different ways. Growth of a thicker oxide dielectric layer surrounding the AlNC metallic core, observed for O_2 and vacuum annealing (Fig. 1E), should redshift the plasmon resonance. But since the oxide layer grows by oxidization of the metallic core (Fig. 2A), and the plasmon resonance frequency of AlNCs depends upon Al core size, reduction of the core diameter should blueshift the plasmon resonance. Consequently, individual dark-field spectra of pre- and postannealed AlNCs should reflect these competing effects.

A characteristic single-particle dark field scattering spectrum, obtained for an individual AlNC before and after O_2 annealing, is shown (Fig. 3A). The O_2 annealing process blueshifts the dipolar plasmon resonance relative to the unannealed resonance at ~ 3.3 eV. O_2 annealing also decreases the magnitude of the quadrupolar plasmon feature at nominally 4.7 to 4.8 eV, consistent with a decrease in Al core size. Thus, the decrease of the Al core size has a greater effect on the plasmonic properties than the oxide growth. To examine the subtleties of these two opposing effects, we obtained dark-field spectra of multiple AlNCs, before and after

O_2 annealing (Fig. 3B). We observe a blueshifted plasmon for this cohort of annealed AlNCs relative to the unannealed case, with statistical variations. The theoretically calculated dipolar plasmon peak maximum for this range of AlNC sizes, for two different oxide thicknesses, is overlaid on the experimental spectral maxima, highlighting the statistical variation observed.

Theoretical spectra allow us to examine the effect of oxide growth distinct from the experimental case where the core size is also simultaneously reduced, showing that this effect alone would produce an easily detectable redshifted plasmon resonance (Fig. 3C). A combination of both oxide layer growth and core size reduction can be modeled by keeping the total size of the Al NC constant, reducing the Al core while increasing the oxide layer thickness (Fig. 3D). This is consistent with our images of AlNCs before and after annealing, where changes in total particle diameter are not typically observed. In this case, the primary modification to the plasmonic response is the decreased amplitude of the quadrupolar plasmon, consistent with our single-particle spectra (Fig. 3A).

NMR Spectroscopy. The types of defects present in the oxide layer are strongly dependent upon the annealing process. Solid-state NMR (ssNMR) spectroscopy was performed to investigate the relative concentrations of the primary alumina coordination states: AlO_4 (tetrahedral), AlO_5 (pentavalent), and AlO_6 (octahedral) (Fig. 4A) (26, 27). Both 4- and 6-coordinate sites are characteristic of crystalline morphologies; the 5-coordinate sites are defect sites with an unsaturated Al valence and a square pyramidal morphology (28, 29). ^{27}Al ssNMR spectra reveal how the three different annealing conditions affect oxide coordination ratios

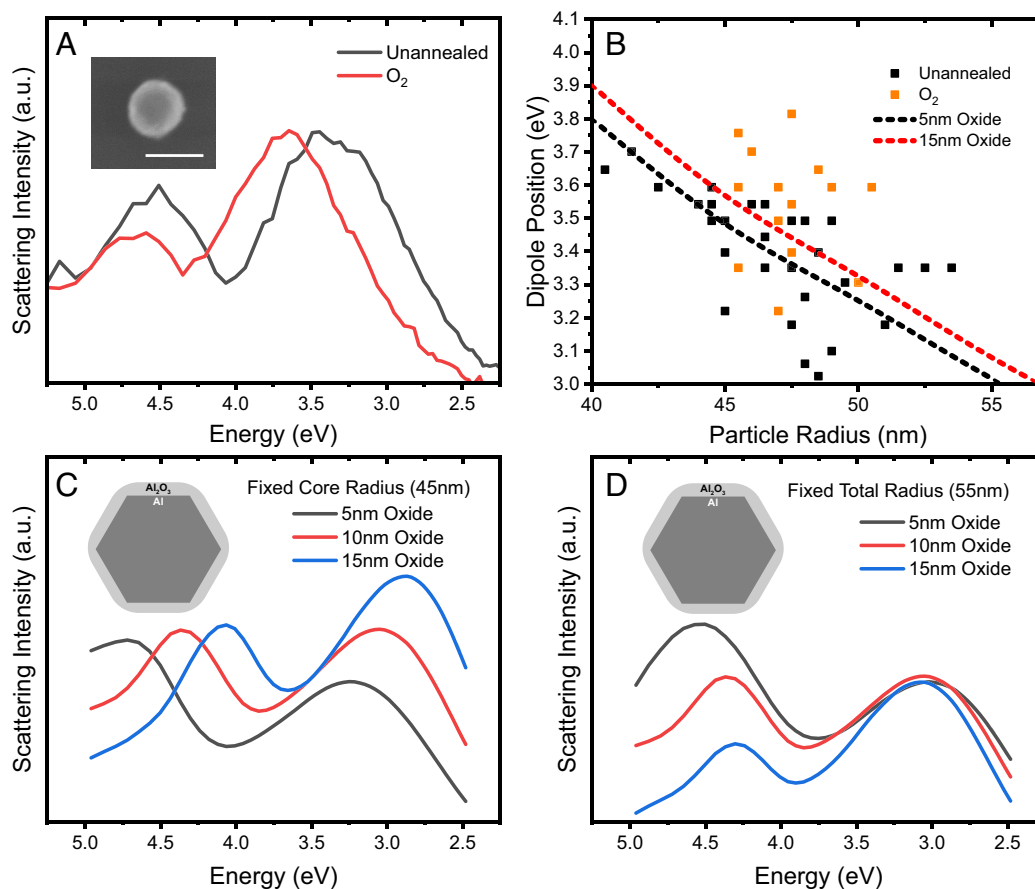


Fig. 3. Plasmonic properties of individual AINCs before and after O₂ annealing. (A) Experimental single-particle scattering spectra of an AINC before and after O₂-annealing. (Inset) Scanning electron microscope image of the AINC after annealing. The scale bar is 100 nm. (B) Plot of measured AINC diameters and corresponding dipole peak positions for a cohort of annealed and unannealed AINCs. Dashed lines represent the calculated dipolar plasmon energies for AINCs with a fixed 5-nm (black) or 15-nm (red) surface oxide layer. (C) Calculated dark-field spectra of a 45-nm fixed radius AINC core with changing shell thicknesses. (D) Calculated dark-field spectra of a 55-nm total radius AINC with changing core radii and oxide layer thicknesses. (C and D, Inset) Schematic of theoretical model for AINC.

(Fig. 4 B–E), quantified by integrating the corresponding ²⁷Al NMR spectral peaks. The unannealed AINCs had weaker NMR signal intensities than the annealed samples, likely due to relative oxide thickness, NMR parameters, or rotor packing (Fig. 4B and SI Appendix, Fig. S9).

The relative concentrations of tetra-, penta-, and hexavalent sites were significantly modified by the various annealing protocols (SI Appendix, Fig. S10). For annealing under a He ambient (Fig. 4C), the relative concentrations of each type of coordination site were nominally equivalent, each at ~30 to 40% of the oxide. This is similar to the unannealed AINCs, except that He-annealed AINCs exhibited a lower relative percentage of 6-coordinate sites. In contrast, following O₂ annealing, the relative contribution of 5-coordinate sites was markedly decreased (Fig. 4D), while after annealing in vacuum, the AINCs exhibited the largest relative fraction of 4- and 5-coordinate sites (Fig. 4E) obtained for all treatments. This was confirmed by cryogenic O₂ pulse chemisorption (SI Appendix, Fig. S11), which allows for quantification of surface defect sites.

Comparison of these spectra to reported ²⁷Al ssNMR spectra of Al polymorphs indicates that the unannealed and He-annealed AINC oxide appear most similar to ρ-alumina, also known as “hydratable alumina,” due to its strong interaction with H₂O to form surface hydroxyl groups (30). The oxide of the O₂-annealed AINCs has a spectrum most similar to γ-alumina, one of the most

studied alumina polymorphs due to its widespread use in thermo-catalysis (31). However, the oxide of the vacuum-annealed AINCs presents a defect-rich spectrum that cannot be attributed to any single naturally occurring alumina phase, to our knowledge. AlO₅-rich 2D materials have been produced by chemical vapor deposition (32) and solvothermal methods (33), but this work represents evidence of predominantly 5-coordinate alumina in colloidal nanocrystals.

Comparing the relative intensities of the metal and oxide peaks in ²⁷Al ssNMR allows for the calculation of total oxide mass within a given AINC powder sample. With this information, we may estimate oxide density (SI Appendix, Note S1). From our analysis, the oxide layer of both the He- and vacuum-annealed AINCs are ~30% less dense than the γ-alumina of the O₂-annealed AINCs, and the unannealed particles are ~72% less dense than the γ-alumina of the O₂-annealed AINCs (SI Appendix, Fig. S12). BET measurements support this large variation in oxide densities, with unannealed AINCs being the most porous, followed by He-, vacuum-, and then O₂-annealed AINCs, in order of decreasing porosity (SI Appendix, Fig. S13).

The relationship between density, phase transition temperature, and defect density of amorphous oxide, the meta-stable polymorphs, and the most thermodynamically stable phase of alumina is summarized in Fig. 5. Literature information regarding the δ-, θ-, and α-phases is shown to provide context, but these polymorphs

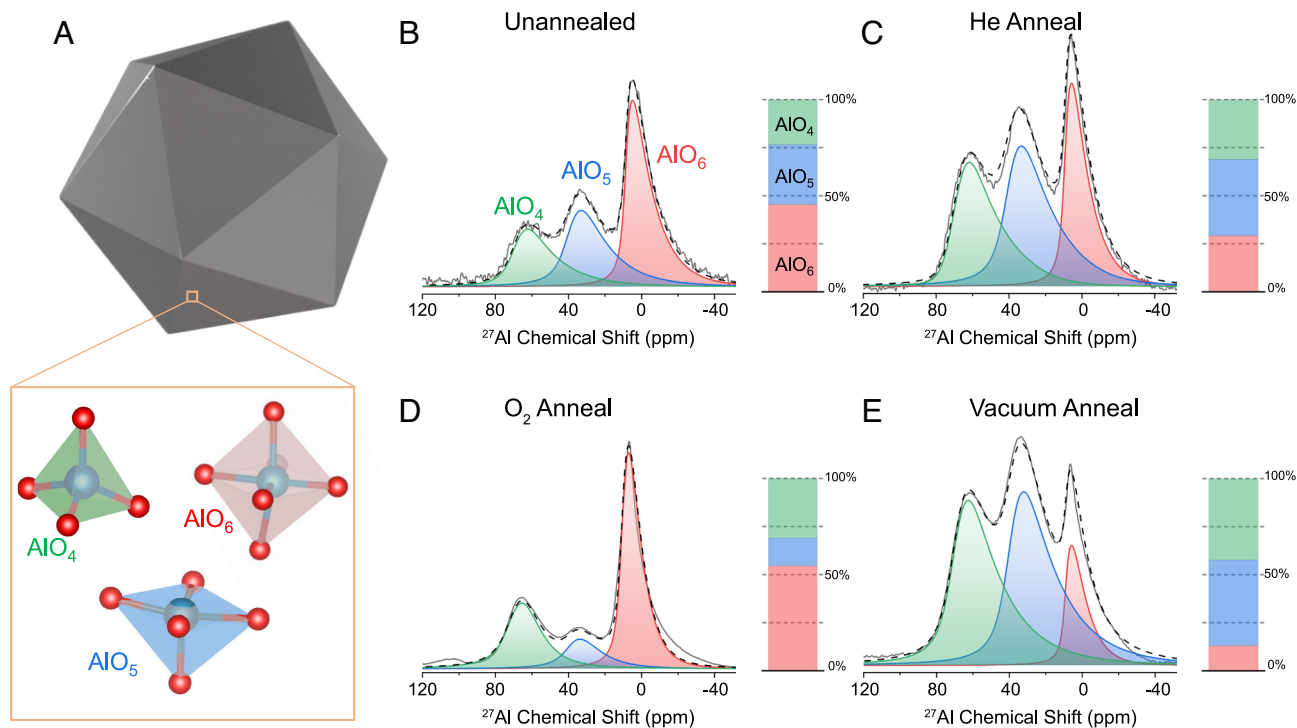


Fig. 4. ^{27}Al ssNMR spectra of AINC oxide following various annealing protocols. (A) AINC illustration showing the most common Al-O coordination states present in the oxide shell. ^{27}Al ssNMR spectra of the oxide region of (B) unannealed AINC, (C) He-annealed AINC, (D) O_2 -annealed AINC, and (E) vacuum-annealed AINC, with accompanying bar plot showing relative quantities of 4-coordinate (green), 5-coordinate (blue), and 6-coordinate (red) alumina sites. The solid gray line represents experimental data, and the dashed black line represents the numerical fit to the data.

are not experimentally observed in this study due to the relatively low annealing temperatures used (7, 27).

Types of Defects induced by Annealing. The concentration and types of active sites present and available are critical for both thermocatalysis and plasmonic photocatalysis, lowering activation barriers for key reactions (34). Acidic sites accept electrons from adsorbates, while basic sites are electron donors (21). Because

pyridine selectively binds to acidic sites and CO_2 binds to basic sites (35), those molecules were used to study chemisorption on the annealed AINC (Fig. 6A). The He-annealed AINC exhibit almost exclusively basic sites, while the vacuum-annealed AINC possess more acidic sites than basic sites. O_2 annealing appears to passivate the surface, exhibiting the fewest active sites resulting from the three types of annealing conditions. Acidic sites on alumina surfaces are attributed to exposed lower-coordination Al

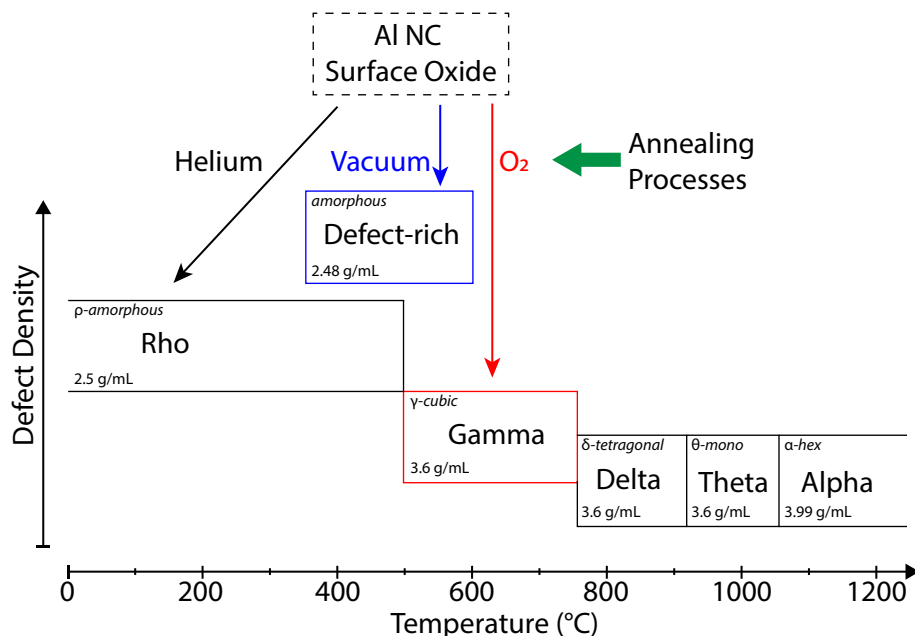


Fig. 5. Schematic representation of the effect of annealing on alumina phase, density, and defect density. The experimentally observed phases in this study (ρ , γ , and defect-rich) are plotted as a function of their transition temperature (x axis) and defect density (y axis) with arrows showing the corresponding annealing ambient. Density and defect information for the high-temperature phases was adapted from refs. 7 and 27, respectively.

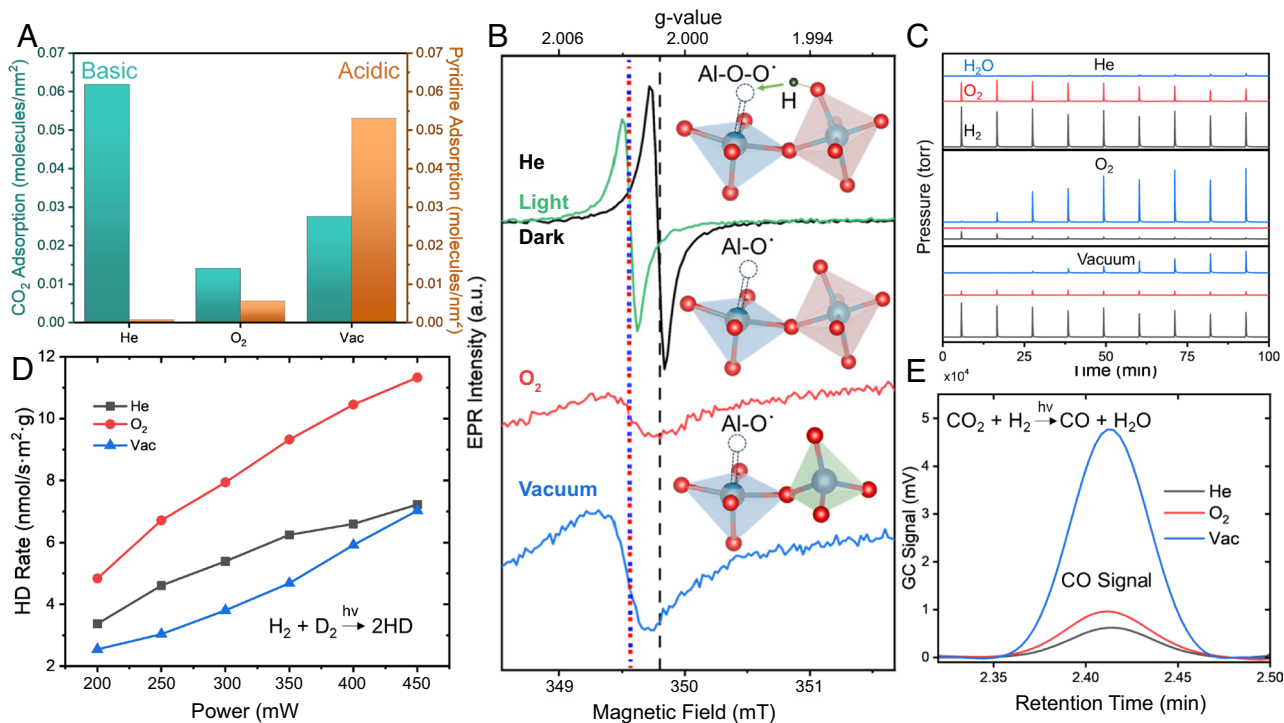


Fig. 6. Variations in defect sites and photocatalytic activity depending upon annealing of AINCs. (A) Measurement of CO₂ and pyridine chemisorption to basic and acidic sites, respectively, on AINCs. (B) X-Band room temperature ssEPR spectra of annealed samples. Above each curve is the proposed structure for surface defect sites in that sample. The green curve represents ssEPR of He-annealed AINCs under illumination, while the blue-red dotted and black dashed vertical lines denote Al-O[•] and Al-O-O[•] defect signals, respectively. (C) Mass spectrometer reading of gas flow over annealed AINCs heated to 500 °C and exposed to pulses of H₂O vapor. (D) Power dependence of photocatalytic H₂ dissociation under broadband illumination. (E) Measurement of GC CO signal during laser illumination.

centers (tetrahedral and defect sites) (36). Basic sites are typically attributed to hydroxyl groups (-OH) formed concomitant with initial oxide growth upon exposure to ambient atmospheric conditions (37). We hypothesize that -OH groups are unaffected by He annealing, effectively creating a protective layer around the AINC that shields the acidic sites from adsorbates. However, O₂ annealing oxidizes the -OH groups, generating H₂O and leaving a surface primarily composed of neutral AlO₆. This is confirmed by mass spectrometry (MS) measurements, which allow for the tracking of desorbed species during He and O₂ annealing (SI Appendix, Fig. S14). At lower annealing temperatures there is substantial desorption of physisorbed H₂O and carbon species for both samples. This is followed by the emergence of an H₂O peak above 480 °C during O₂ annealing which gradually returns to baseline levels, indicating oxidation of the hydroxyl sites. No H₂O was observed at elevated temperatures for the He-annealed AINCs during the annealing process. Some exposed tetrahedral sites and remaining hydroxyl groups account for the low but measurable active site populations on O₂-annealed AINCs. Vacuum annealing appears to remove the O atoms from the oxide lattice through dehydroxylation and dehydration, which simultaneously generate lower coordination sites and remove many surface -OH groups, allowing adsorbates to interact with the now-exposed acidic sites (38). The effect of annealing for each ambient condition is summarized in SI Appendix, Fig. S15.

Solid-state electron paramagnetic resonance (ssEPR) was used to probe the interaction of electrons with active sites on the AINC surface. The measured ssEPR spectrum of He-annealed AINCs indicates the presence of electrons occupying pentavalent defect sites stabilized by adjacent -OH groups (Al-O-O[•] sites) at the surface (Fig. 6 B, Top) (39). In contrast, the spectra of both O₂- and vacuum-annealed AINCs indicate electrons localized at pentavalent defects (Al-O[•] sites) with no neighboring hydroxyl groups

(Fig. 6 B, Middle and Bottom) (39). When O₂- and vacuum-annealed samples are illuminated with a broadband visible light source, they exhibit no light-induced changes (SI Appendix, Fig. S16). However, when He-annealed AINCs are illuminated, the spectrum shifts and decreases to become more similar to the spectra of the O₂- and vacuum-annealed AINCs. This light-induced shift, which possesses an extremely long relaxation time (hours), is quite possibly related to a spin-forbidden relaxation from an excited state of the pentavalent site to its ground state, and merits further study.

Catalytic Properties. To probe how changes to the AINC surface oxide affect catalytic behavior, several chemical reactions were investigated (Fig. 6 C-E). Vapor-phase thermocatalytic water splitting was chosen due to its reliance on different active sites for both oxygen and hydrogen evolution (40). AINCs were heated to 500 °C under He gas flow followed by exposure to controlled pulses of H₂O vapor in the He carrier gas: desorbed H₂O and the O₂ and H₂ produced were measured by MS (Fig. 6C). For the He-annealed AINCs, high levels of both O₂ and H₂ and the absence of H₂O in the product stream during the first five pulses indicate water splitting facilitated by the surface oxide layer. After that, the O₂ decreases and H₂O increases with each pulse, most likely indicating a subsequent slow oxidation of the Al core. The vacuum-annealed sample initially produced H₂, but with little O₂ generated and a delayed, slow rise in H₂O. This indicates that H₂O molecules quickly oxidized the surface defects, then likely started oxidizing the Al core. For the O₂-annealed AINCs, the H₂O signal rises rapidly, but there is no O₂ observed, and the weak H₂ signal disappears after the first few H₂O pulses. It is likely that the crystalline oxide protects the core from oxidation but, perhaps due to its strongly reduced density of defect sites, also does not contribute to catalysis. We conclude that the basic

sites present on the He-annealed AINC surface show a capacity for thermocatalytic splitting of water, while the crystalline oxide generated by O₂ annealing enhances AINC stability.

Next, we explored the influence of surface oxide annealing on the plasmonic H₂ dissociation through the probe reaction of HD exchange (H₂ + D₂ → 2HD) (Fig. 6D). Our previous study of this light-induced reaction on AINCs suggested that injection of a nonequilibrium hot electron into the antibonding orbital of H₂ could facilitate its dissociation on AINCs, in direct analogy to HD exchange on plasmonic Au nanoparticles (41). For AINCs, the surface oxide layer is sufficiently porous to allow H₂ (and D₂) diffusion to the Al metal core surface, allowing hot electron transfer from metal to adsorbate molecule to occur (41). Here, we observed an increase in the HD production rate for all three catalysts with increasing light intensity from a pulsed broadband laser source (Fianium). The O₂-annealed AINCs showed slightly better photocatalytic activity toward H₂ dissociation than the vacuum- and He-annealed AINCs. Since this reaction occurs at the Al interface, where a hot electron can transfer into the H₂ LUMO orbital, this variation in reactivity probes differences in diffusion of H₂ through the different surface oxides. The differences in reactivity observed likely indicate that H₂ diffusion through the vacuum-annealed and He-annealed alumina polymorphs is slightly reduced by the presence of disorder in those oxides relative to the substantially more crystalline γ -alumina (42).

While stoichiometric oxides generally exhibit low H₂ diffusion and uptake capacity, the presence of defects in the oxide layer (i.e., the amorphous alumina layer) was previously demonstrated to substantially enhance H₂ uptake and transportation through alumina (43). In light of those previous results, the observed HD exchange reactivity trend in the annealed AINCs appears quite surprising, since the vacuum-annealed catalyst with the highest defect density from unsaturated Al(V) sites (Fig. 4) would be expected to show a higher reactivity compared to the O₂-annealed catalyst with fewer oxide defects. However, the observed photocatalytic reactivity trend implies that hot-electron transfer and injection into the H₂ LUMO orbital at the Al interface could play a key role on determining the outcome of photocatalysis, largely independent of oxide defect density.

The reverse water–gas shift reaction (rWGS) was also tested due to its importance for generating fuel from greenhouse gases and its known preference for basic catalytic sites under thermocatalytic conditions (44). Under white light illumination with no external heating, vacuum-annealed AINCs exhibited a substantially higher photocatalytic CO production rate compared to the other catalysts with almost similar reactivity, as measured by gas chromatography (GC) (Fig. 6E). To probe this behavior, we performed CO₂ physisorption experiments (SI Appendix, Fig. S17), which showed the highest CO₂ uptake for He-annealed AINCs, followed by vacuum- and then O₂-annealed AINCs, in accordance with the relative abundance of basic sites in Fig. 6A. In contrast, the photocatalytic rWGS rates better correlate with the concentration of acidic sites, not with the concentration of basic sites in Fig. 6A (vacuum > O₂ > He). This is quite possible, since CO₂ can also adsorb at surface defect sites formed by dehydroxylation (Lewis acid sites) (45). Consequently, it appears that the trend in photocatalytic activity is not determined solely by differences in CO₂ adsorption: the photoexcitation of AINCs also affects the observed relative catalytic activities. We hypothesize that while basic sites provide adsorption sites for CO₂, plasmonic hot electron generation drives H₂ dissociation at the Al core surface, followed by the possibility of H₂- or H atoms diffusing to the CO₂ binding sites to generate CO and H₂O. It is possible that the combination of high defect density and the presence of hot electron-generated reactive H atoms or

H₂- intermediates may make the vacuum-annealed AINCs the most effective of these photocatalysts for the rWGS reaction. Although the high degree of oxide crystallinity of O₂-annealed AINCs eliminated most defects, its moderate activity is caused by its retention of some basic sites and its ability to facilitate hot electron-driven H₂ dissociation. Although He-annealed AINCs have many basic sites, it is possible that the high concentration of surface hydroxyl groups may screen the interaction of adsorbates with those defect sites, leading to less photocatalytic activity. While the precise reaction mechanism would require extensive further study, this reaction illustrates how tailoring defects in surface oxides provides different reaction pathways in plasmonic photocatalysis relative to thermocatalytic approaches.

Discussion and Conclusions

We have shown that the native surface oxide of colloiddally synthesized AINCs can be altered by annealing under various conditions, modifying many of its properties. Our work demonstrates that thermal annealing under various ambient gases can dramatically modify the type and concentration of defects in and on the surface oxide, which in turn modifies their behavior as reactive sites under thermocatalytic and plasmonic photocatalytic conditions. This simple approach can be expanded to tailor the properties of a much wider range of metal oxides, grown onto plasmonic nanoparticle surfaces, to facilitate plasmonic photocatalysts for a wider range of chemical reactions yet to be studied.

Materials and Methods

AINC Preparation. All chemicals were purchased from Sigma-Aldrich unless otherwise noted. Dimethylethylamine alane (DMEAA) was obtained as 0.5 M solution in toluene. 1,4-dioxane and tetrahydrofuran (THF) and toluene were dried and sparged using a solvent system. High purity titanium (IV) isopropoxide (99.99%) was used. All above reagents and solvents for AINC synthesis were handled under an inert atmosphere using a glovebox. ACS Grade isopropanol (IPA) was used. All glassware was dried in an oven at 120 °C before use. In an argon-filled glovebox, 80 mL 1,4-dioxane in a stoppered 250 mL Erlenmeyer flask was stirred vigorously for at least an hour with the hot plate set to 45 °C to ensure temperature uniformity. Twenty mL of DMEAA was added and stirred for 30 min. Two mL of titanium (IV) isopropoxide (50 mM in toluene) was added, turning the solution from clear to brown immediately and then slowly proceeding to black and gray. The reaction proceeded for 24 h and was quenched by the addition of 100 mL toluene. Products were removed from the glovebox and sonicated in loosely capped centrifuge tubes. AINCs were isolated by multiple centrifugation cycles in IPA and then dried under house vacuum until solvent completely evaporated. At this scale, synthesis yields 200 to 240 mg of AINC powder. Larger particles can be obtained by using a mixture of 1,4-dioxane and THF in place of pure 1,4-dioxane.

AINC Treatment. The dried AINC powder was ground in a mortar and pestle to break up aggregates and then divided into separate vials. He and O₂ annealing was performed in an AutoChem II 2920 using UHP He and 10% O₂ in He from Airgas. For He annealing, samples were ramped in 50 sccm He flow at 30 °C/min, and then held at 500 °C for 1 h before being cooled via liquid nitrogen pump at 30 °C/min to ambient temperature. For O₂ annealing, samples were ramped in He at 30 °C/min to 500 °C. Once maximum temperature was achieved, O₂ flow was introduced into the system for 1 h. Then, the O₂ flow was replaced by He before the 30 °C/min cooling ramp began. Vacuum annealing was performed in an MTI 53L vacuum oven with attached mechanical pump, generating 10⁻² torr vacuum. The sample was heated to 500 °C at 1 °C/min, and then held at 500 °C for 1 h before being cooled back to room temperature.

Material Characterization. Solid-state NMR measurements were performed on a 500-MHz Bruker AVIII HD wide-bore spectrometer with a zirconia 4 mm rotor at a spin rate of 12 KHz at a 10-degree pulse. Fitting was completed using Cjzek distribution on the ssNake software, a cross-platform open-source NMR data processing and fitting application (46). EPR measurements at X-Band ~9.8 GHz

were performed on a Bruker ELEXSYS E500 spectrometer fitted with an ER4102ST resonator at room temperature using a 4 mm quartz sample holder. Illuminated EPR experiments were performed using a 150W Xe arc lamp coupled to a fiber that aligned into the optical port of the ER4102ST resonator at room temperature using a 4-mm quartz sample holder. TEM imaging was performed on a JEOL 2100F transmission electron microscope operating at 200 kV. HAADF-STEM, EDX, and 4D-STEM measurements were performed at 300 kV on an FEI Titan Themis3 (scanning) transmission electron microscope (S/TEM) equipped with EMPAD detector. XRD measurements were performed on a Rigaku Smartlab II with zero-background sample holder. Extinction spectra were measured on a Cary 5000 UV/Vis/NIR spectrometer.

Chemisorption and Physisorption. All chemisorption experiments were performed on an AutoChem II 2920 equipped with thermal conductivity detector and online mass spectrometer (MKS Cirrus II). Annealed samples (50 to 80 mg) were introduced into the U-shaped sample tube and treated in 50 sccm He for one hour at 500 °C to remove any adsorbed water and atmospheric contaminants. For basic site measurements, the sample was ramped to 45 °C under 40 sccm He, and then exposed to 0.5 mL pulses of 10% CO₂ in He (Airgas) until saturation. For acidic site measurements, the sample was ramped to 120 °C, and a vapor generator set to 90 °C was used to introduce pulses of anhydrous pyridine (Sigma Aldrich) until saturation. For O₂ chemisorption, the sample was cooled to -90 °C and then exposed to pulses of 10% O₂ in He. For H₂O vapor splitting, the sample was ramped to 500 °C and a vapor generator set to 85 °C was used to introduce 0.5 mL pulses of MilliQ H₂O. Pore volume and CO₂ uptake were measured using a Quantachrome Autosorb-iQ3-MP/Kr BET Surface Analyzer at 273 K up to 1 bar. Samples were degassed for 4 h under vacuum at 150 °C prior to measurement.

Catalysis. The nanoparticles were mixed with Aerosil SiO₂ support particles at 10% loading, and the mixture was ground thoroughly to homogenize the catalyst. All catalytic activities were measured at a total pressure of 1 atm using about 10 mg of the catalyst loaded into a customized stainless-steel chamber flow fixed-bed reactor (Harrick Scientific Products Inc.). The photocatalytic experiments were performed at room temperature without external heating. The catalyst was illuminated using a supercontinuum fiber laser (6 ps, 80 MHz; Fianium) with 750 nm shortpass and no focusing lens. For the rWGS reaction, a 1:1 ratio of CO₂/H₂ (research purity, Airgas) was continuously flowed into the reaction chamber at a total flow rate of 20 sccm. For hydrogen dissociation, a 1:1 ratio of H₂/D₂ was flowed instead. The effluent composition was measured using a customized gas chromatograph (Shimadzu) equipped with a pulsed discharge helium ionization detector (for rWGS) and Hiden online mass spectrometer (for H₂ dissociation).

4D-STEM Data Acquisition. The 4D-STEM datasets were taken on an aberration-corrected FEI Titan Themis with an Electron Microscope Pixel Array Detector (EMPAD). As the focused electron beam scans over an AINC sample, a diffraction pattern is recorded at each scan position by the EMPAD. Due to its high dynamic range (1,000,000:1), lattice strain can be measured with subpicometer precision through the diffraction. The 4D datasets of the AINC were acquired at 300 kV. A 1.76-mrad convergence angle was used, leading to a ~0.69-nm probe size. For a 300 kV electron beam, 579 ADUs represent one electron per pixel. For all the datasets, an exposure time of 1.86 ms (1 ms acquisition time along with 0.86 ms readout time) was employed when acquiring the EMPAD 4D datasets. The scan size in real space (the number of pixels the beam scans across) can be set from 64 × 64 to 512 × 512. The scan size of the data used in this work was 256 × 256.

4D-STEM Data Processing. Domains with different lattice orientations in the 4D-STEM datasets are first segmented through unsupervised hierarchical clustering and we map the strain of each domain individually (SI Appendix, Fig. S18) (47). To avoid the dynamical multiscattering and the lattice mistilt, we utilized the exit-wave power-cepstrum (EWPC) method to measure the lattice strain (48). The raw diffraction patterns are transformed as logarithmic intensity scale first and then the power cepstrum image will be calculated as the fast Fourier transform (FFT) of the log scale diffraction (SI Appendix, Fig. S19). Since the diffraction pattern is in reciprocal space, the power cepstrum, which is FFT of diffraction, is transformed back to real space. Therefore, the real space lattice vector a_i can be directly measured in each cepstrum image. Subsequently, the transformation matrix T can be calculated through $a_i = Ta_{unstrained}$. Through

polar decomposition, the transformation matrix T can be separated into a rotation matrix R and a strain matrix U . The in-plane uniaxial strain can be computed by $e_{xx} = 1 - U_{00}$, $e_{yy} = 1 - U_{11}$, and the shear strain and rotation can be calculated by $e_{xy} = 1 - U_{01}$ and $\theta = \cos^{-1}R_{00}$. The biaxial strain shown in Fig. 2 can be calculated by $(e_{xx} + 1)(e_{yy} + 1) - 1$, which represent the Al lattice size changes compared with the unstrained reference.

Fluctuation electron microscopy (FEM) images are measured by the normalized variance of the cepstrum intensity in the medium-range order (SI Appendix, Fig. S20) (25, 49). The anisotropy crystalline regions with strong peaks give higher FEM score while the isotropy disordered regions with uniform amorphous rings give lower FEM score.

Dark-Field Scattering. Fused silica substrates from Silicon Valley Microelectronics were cleaned by sonication in acetone followed by a rinse with isopropanol (IPA). A correlation grid was formed by deposition of a 50-nm Au layer with a 2-nm Ti adhesion layer through a TEM grid with no carbon film (Ted Pella Micron Index 1). Particle samples were diluted in IPA to an appropriate degree and then ~10 μL was drop-cast onto a prepared substrate. Reflection-mode measurements were carried out using a custom-built instrument capable of measuring from 225 to 700 nm. Measurements were taken with a 5-nm step size and an integration time of 15 to 20 s. Correlation was done with SEM on an FEI Quanta 650.

Optical Simulations. Dark-field scattering simulations were performed with the finite-difference time-domain (FDTD) method (Lumerical Solutions 2023 R1.3). Aluminum cuboctahedrons were modeled with rounded edges of 10-nm radius of curvature. The aluminum cuboctahedrons were surrounded with a 5-, 10-, or 15-nm-thick oxide layer with rounded edges of the same radius of curvature. The particles are on top of quartz substrate. A single frequency total-field scattered-field approach was used to obtain dark-field scattering spectra at a 60° angle from substrate normal. The cuboctahedron is aligned such that light is incident on a face of the cuboctahedron. Scattering cross-sections in simulations were calculated by integration of corresponding far-field differential scattering cross-sections in a hollow cone 8-16° from substrate normal. The energy range was swept over from 2.5 to 5 eV, and the permittivity of each material at the simulated energies was interpolated from corresponding dielectric functions. For the aluminum core, alumina shell, and silica substrate, Palik's optical constant data were used. The external medium on the incident side was assumed to be vacuum. A 1.5-nm mesh size was used for scattering cross-section simulations. Far-field scattering patterns were calculated with a custom program, based on the Schelkunoff equivalence theorem and the Lorentz reciprocity principle, that performs the near-to-far field transformation of equivalent electric and magnetic currents on a closed surface enclosing the nanoparticle. Equivalent currents were derived from fields calculated using Lumerical FDTD.

Data, Materials, and Software Availability. All study data are included in the article and/or SI Appendix.

ACKNOWLEDGMENTS. We gratefully acknowledge the support of our research from the Air Force Office of Scientific Research under Grant no. FA9550-15-1-0022, the Defense Threat Reduction Agency under Grant no. HDTRA1-16-1-0042, NSF NEWT (EEC-1449500), NSF under Grant no. DMR-1905757 (G.F.S.), and the Robert A. Welch Foundation under Grant Nos. C-1220 (N.J.H.), C-1222 (P.N.), and C-2065 (Y.H.). C.J.F. acknowledges support from the Department of Defense SMART Scholarship under OUSD/R&E, NDEP/BA-1, and Y.M.C. acknowledges support from Fulbright Colombia-Pasaporte a la Ciencia. C.S. and Y.H. also acknowledge support from NSF (CMMI-2239545). We further acknowledge the use of the Rice University Shared Equipment Authority facilities, most notably the Electron Microscopy Center, the use of the Materials Characterization Laboratory (FSU075000MAC) and the SSNMR laboratory (NSF-CHE1126587) at the Florida State University Department of Chemistry and Biochemistry.

Author affiliations: ^aDepartment of Chemistry, Rice University, Houston, TX 77005; ^bLaboratory for Nanophotonics, Rice University, Houston, TX 77005; ^cDepartment of Chemistry, Florida State University, Tallahassee, FL 32306; ^dDepartment of Materials Science and NanoEngineering, Rice University, Houston, TX 77005; ^eDepartment of Physics & Astronomy, Rice University, Houston, TX 77005; ^fDepartment of Electrical and Computer Engineering, Rice University, Houston, TX 77005; and ^gArmy Development Command Army Research Laboratory-South, Rice University, Houston, TX 77005

- X. L. Liu *et al.*, Deactivation and regeneration of Claus catalyst particles unraveled by pore network model. *Chem. Engineering Sci.* **211**, 115305 (2020), 10.1016/j.ces.2019.115305.
- A. Aghaeinejad-Meybodi, A. Ebadi, S. Shafiei, A. Khataee, A. D. Kiadehi, Degradation of Fluoxetine using catalytic ozonation in aqueous media in the presence of nano-gamma-alumina catalyst: Experimental, modeling and optimization study. *Sep. Purif. Technol.* **211**, 551–563 (2019), 10.1016/j.seppur.2018.10.020.
- W. Lee, R. Ji, U. Gosele, K. Nielsch, Fast fabrication of long-range ordered porous alumina membranes by hard anodization. *Nat. Mater.* **5**, 741–747 (2006), 10.1038/nmat1717.
- M. Iwai, T. Kikuchi, R. O. Suzuki, Self-ordered nanospire porous alumina fabricated under a new regime by an anodizing process in alkaline media. *Sci. Rep.* **11**, 7240 (2021), 10.1038/s41598-021-86696-z.
- N. H. A. Besisa, D. H. A. Besisa, E. M. M. Ewais, Processing of high temperature alumina/aluminum titanate ceramic composites from clean sources. *Sci. Rep.* **12**, 5957 (2022), 10.1038/s41598-022-09670-3.
- G. Busca, *Advances in Catalysis*, F. C. Jentoft, Ed. (2014), vol. 57, pp. 319–404.
- I. Levin, D. Brandon, Metastable alumina polymorphs: Crystal structures and transition sequences. *J. Am. Ceramic Soc.* **81**, 1995–2012 (1998).
- Z. Lodziana, N. Y. Topsoe, J. K. Norskov, A negative surface energy for alumina. *Nat. Mater.* **3**, 289–293 (2004), 10.1038/nmat1106.
- B. E. Leach, *Applied Industrial Catalysis*, B. E. Leach, Ed. (Academic Press, 1983), pp. 1–30.
- H. Knozinger, P. Ratnasamy, Catalytic aluminas—Surface models and characterization of surface sites. *Catalysis Rev. Sci. Engineering* **17**, 31–70 (1978), 10.1080/03602457808080878.
- M. L. Brongersma, N. J. Halas, P. Nordlander, Plasmon-induced hot carrier science and technology. *Nat. Nanotechnol.* **10**, 25–34 (2015), 10.1038/nnano.2014.311.
- C. Zhang *et al.*, Al-Pd nanodisk heterodimers as antenna-reactor photocatalysts. *Nano Lett.* **16**, 6677–6682 (2016), 10.1021/acs.nanolett.6b03582.
- L. A. Zhou *et al.*, Quantifying hot carrier and thermal contributions in plasmonic photocatalysis. *Science* **362**, 69 (2018), 10.1126/science.aat6967.
- L. A. Zhou *et al.*, Light-driven methane dry reforming with single atomic site antenna-reactor plasmonic photocatalysts. *Nat. Energy* **5**, 61–70 (2020), 10.1038/s41560-019-0517-9.
- M. W. Knight *et al.*, Aluminum for plasmonics. *ACS Nano* **8**, 834–840 (2014), 10.1021/nn405495q.
- R. Sundararaman, P. Narang, A. S. Jermyn, W. A. Goddard, H. A. Atwater, Theoretical predictions for hot-carrier generation from surface plasmon decay. *Nat. Commun.* **5**, 5788 (2014), 10.1038/ncomms6788.
- D. F. Swearer *et al.*, Heterometallic antenna-reactor complexes for photocatalysis. *Proc. Natl. Acad. Sci. U.S.A.* **113**, 8916–8920 (2016), 10.1073/pnas.1609769113.
- A. Bayles *et al.*, Al@TiO₂ core-shell nanoparticles for plasmonic photocatalysis. *ACS Nano* **16**, 5839–5850 (2022), 10.1021/acsnano.1c10995.
- M. J. McClain *et al.*, Aluminum nanocrystals. *Nano Lett.* **15**, 2751–2755 (2015), 10.1021/acs.nanolett.5b00614.
- C. R. Jacobson *et al.*, Shining light on aluminum nanoparticle synthesis. *Acc. Chem. Res.* **53**, 2020–2030 (2020), 10.1021/acs.accounts.0c00419.
- J. M. Campelo, A. Garcia, J. M. Gutierrez, D. Luna, J. M. Marin, Alkali-promoted AlPO₄ catalysis. 1. Acid-base and oxidizing-reducing properties. *J. Colloid Interf. Sci.* **95**, 544–550 (1983), 10.1016/0021-9797(83)90213-8.
- Y. M. Han *et al.*, Strain mapping of two-dimensional heterostructures with subpicometer precision. *Nano Lett.* **18**, 3746–3751 (2018), 10.1021/acs.nanolett.8b00952.
- M. W. Tate *et al.*, High dynamic range pixel array detector for scanning transmission electron microscopy. *Microsc. Microanal.* **22**, 237–249 (2016), 10.1017/s1431927615015664.
- B. D. Clark *et al.*, Aluminum nanocubes have sharp corners. *ACS Nano* **13**, 9682–9691 (2019), 10.1021/acsnano.9b05277.
- P. M. Voyles, D. A. Muller, Fluctuation microscopy in the STEM. *Ultramicroscopy* **93**, 147–159 (2002), 10.1016/S0304-3991(02)00155-9.
- S. K. Lee, S. B. Lee, S. Y. Park, Y. S. Yi, C. W. Ahn, Structure of amorphous aluminum oxide. *Phys. Rev. Lett.* **103**, 095501 (2009), 10.1103/PhysRevLett.103.095501.
- C. V. Chandran *et al.*, Alumina: Discriminative analysis using 3D correlation of solid-state NMR parameters. *Chem. Soc. Rev.* **48**, 134–156 (2019), 10.1039/c8cs00321a.
- J. H. Kwak *et al.*, Coordinatively unsaturated Al³⁺ centers as binding sites for active catalyst phases of platinum on gamma-Al₂O₃. *Science* **325**, 1670–1673 (2009), 10.1126/science.1176745.
- Z. C. Zhao *et al.*, Nature of five-coordinated Al in gamma-Al₂O₃ revealed by ultra-high-field solid-state NMR. *ACS Central Sci.* **8**, 795–803 (2022), 10.1021/acscentsci.1c01497.
- R. H. Meinhold, R. C. T. Slade, R. H. Newman, High-field MAS NMR, with simulations of the effects of disorder on lineshape, applied to thermal transformations of alumina hydrates. *Appl. Magn. Reson.* **4**, 121–140 (1993), 10.1007/bf03162559.
- G. I. N. Waterhouse *et al.*, Structural, optical, and catalytic support properties of gamma-Al₂O₃ inverse opals. *J. Phys. Chem. C* **119**, 6647–6659 (2015), 10.1021/acs.jpcc.5b00437.
- L. Baggetto *et al.*, Atomic scale structure of amorphous aluminum oxyhydroxide, oxide and oxycarbide films probed by very high field Al-27 nuclear magnetic resonance. *Phys. Chem. Chem. Phys.* **19**, 8101–8110 (2017), 10.1039/c6cp07937g.
- L. Shi *et al.*, Al₂O₃ nanosheets rich in pentacoordinate Al³⁺ ions stabilize Pt-Sn clusters for propane dehydrogenation. *Angew. Chem. Int. Ed. Engl.* **54**, 13994–13998 (2015), 10.1002/anie.201507119.
- A. Corma, H. Garcia, Lewis acids: From conventional homogeneous to green homogeneous and heterogeneous catalysis. *Chem. Rev.* **103**, 4307–4365 (2003), 10.1021/cr030680z.
- J. L. G. Fierro, L. G. Tejuca, Surface interactions of carbon-dioxide and pyridine with LaCrO₃ perovskite-type oxide. *J. Chem. Technol. Biotechnol. Chem. Technol.* **34**, 29–37 (1984).
- D. Coster, A. L. Blumenfeld, J. J. Fripiat, Lewis-acid sites and surface aluminum in aluminas and zeolites—A high-resolution NMR-study. *J. Phys. Chem.* **98**, 6201–6211 (1994), 10.1021/j100075a024.
- P. E. Hoggan, A. Aboulayt, A. Pieplu, P. Nortier, J. C. Lavalley, Mechanism of COS hydrolysis on alumina. *J. Catalysis* **149**, 300–306 (1994), 10.1006/jcat.1994.1298.
- I. V. Gasenkova, N. I. Mukhurov, S. P. Zhvavi, E. E. Kolesnik, A. P. Stupak, Effect of heat treatment in vacuum on photoluminescence of anodic alumina. *Luminescence* **34**, 520–525 (2019), 10.1002/bio.3670.
- T. Ishizaka, S. Tero-Kubota, Y. Kurokawa, T. Ikoma, EPR studies on defects in sol-gel derived alumina films. *J. Phys. Chem. Solids* **64**, 801–806 (2003), 10.1016/s0022-3697(02)00377-3.
- N. Seal, A. Karmakar, S. Kundu, S. Neogi, Undulated Ni(II)-framework with in situ-grafted open-metal and basic sites for high-performance electrochemical water oxidation and flexible composite-driven size-exclusive autotandem catalysis. *ACS Sustain. Chem. Engg.* **11**, 979–993 (2023), 10.1021/acssuschemeng.2c05673.
- L. Zhou *et al.*, Aluminum nanocrystals as a plasmonic photocatalyst for hydrogen dissociation. *Nano Lett.* **16**, 1478–1484 (2016), 10.1021/acs.nanolett.5b05149.
- L. S. Salomone, F. Campabadal, A. Faigon, Electron trapping in amorphous Al₂O₃. *J. Appl. Phys.* **123**, 085304 (2018), 10.1063/1.5005546.
- Y. Wang, G. K. Palsson, H. Raanaei, B. Hjorvarsson, The influence of Al₂O₃ coating on hydrogen uptake of materials. *J. Alloys Comp.* **464**, L13–L16 (2008).
- M. Gonzalez-Castano, B. Dorneanu, H. Arellano-Garcia, The reverse water gas shift reaction: A process systems engineering perspective. *React. Chem. Eng.* **6**, 954–976 (2021), 10.1039/d0re00478b.
- J. Szanyi, J. H. Kwak, Dissecting the steps of CO₂ reduction: 1. The interaction of CO and CO₂ with γ -Al₂O₃: An in situ FTIR study. *Phys. Chem. Chem. Phys.* **16**, 15117 (2014).
- S. G. J. van Meerten, W. M. J. Franssen, A. P. M. Kentgens, ssNake: A cross-platform open-source NMR data processing and fitting application. *J. Magn. Reson.* **301**, 56–66 (2019), 10.1016/j.jmr.2019.02.006.
- C. Shi *et al.*, Uncovering material deformations via machine learning combined with four-dimensional scanning transmission electron microscopy. *npj Comput. Mater.* **8**, 114 (2022), 10.1038/s41524-022-00793-9.
- E. Padgett *et al.*, The exit-wave power-spectrum transform for scanning nanobeam electron diffraction: Robust strain mapping at subnanometer resolution and subpicometer precision. *Ultramicroscopy* **214**, 112994 (2020), 10.1016/j.ultramic.2020.112994.
- S. Pidaparthi, H. Ni, H. Hou, D. P. Abraham, J.-M. Zuo, Fluctuation cepstral scanning transmission electron microscopy of mixed-phase amorphous materials. *Ultramicroscopy* **248**, 113718 (2023), 10.1016/j.ultramic.2023.113718.